

Article

Dynamic Mechanical Behavior and Microstructure Evolution of an Extruded 6013-T4 Alloy at Elevated Temperatures

Tuo Ye ^{1,2,3}, Yuanzhi Wu ¹, Wei Liu ¹, Bin Deng ¹, Anmin Liu ¹ and Luoxing Li ^{1,2,3,*}

¹ Research Institute of Automobile Parts Technology, Hunan Institute of Technology, Hengyang 421002, China; yetuo@hnu.edu.cn (T.Y.); ranco007@163.com (Y.W.); hitliuwei1105@163.com (W.L.); Dengbinbin1981@126.com (B.D.); liuanmin63@163.com (A.L.)

² State Key Laboratory of Advanced Design and Manufacturing for Vehicle Body, Hunan University, Changsha 410082, China

³ College of Mechanical and Vehicle Engineering, Hunan University, Changsha 410082, China

* Correspondence: luoxing_li@yahoo.com; Tel.: +86-0731-88821571; Fax: +86-0731-88822051

Received: 6 May 2019; Accepted: 29 May 2019; Published: 30 May 2019



Abstract: The mechanical properties of an extruded 6013-T4 alloy were tested at a temperature range from 25 to 400 °C and strain rate range from 1×10^3 to 5×10^3 s⁻¹. The results demonstrate that the stress level is sensitive to strain rate and temperature. The stress level increases slightly with increasing strain rate and decreases remarkably with increasing temperature. The dislocation and precipitate undergo great changes. When deformed at 25 °C, the density of the dislocation increases with strain and strain rate; which leads to a higher stress level. A great number of needle-like precipitates were observed at samples deformed at 200 °C. It is clear that the density of dislocation increases with strain and strain rate. When impacted at 400 °C, the coarser precipitates were found in the specimen; the density of the dislocation increases with strain and strain rate.

Keywords: 6013 alloy; high strain rate impact; mechanical property; microstructure evolution

1. Introduction

Aluminum alloy possesses excellent mechanical properties, such as high specific strength, outstanding forming ability, and at the same time it has a low cost and attractive scrap compatibility [1–3]. In recent years, a number of aluminum alloys have been contrived by adding different element contents. As a result, each series of the alloys exhibits unique mechanical properties. The Al-Mg-Si alloy is a kind of aging hardenable alloy, and Mg and Si atoms are the main constituent elements for the precipitate [4]. The general precipitation sequence has been accepted as: α (SSSS) \rightarrow clusters \rightarrow GP (Guinier–Preston) zones $\rightarrow \beta'' \rightarrow \beta' \rightarrow \beta$ It has been reported that the type, dimension, and density of the precipitate has a great influence on the strength and plasticity of the alloy. Meanwhile, the precipitate evolution also has a great effect on the performance of the alloys [5]. The Al-Mg-Si alloy owns excellent performance and is commonly used in many fields. It is applied for many automobile components such as racks, bumpers, and seats in the automotive industry [6]. In the aircraft field, this alloy is employed to make structural parts, namely, fuselages and wings [7]. It is acclaimed that the Al-Mg-Si alloy is used in the manufacture of watercraft, in consideration of its low density, medium level of strength, and excellent corrosion resistance in the marine industry [8]. The usage of the Al-Mg-Si alloy has continued to grow in the manufacturing of structural parts that are used for bearing critical loading in the past decade [9].

The as-extruded Al-Mg-Si alloys are usually subjected to various dynamic impact loads [10–12]. On the one hand, with increasing requirements of produce efficiency, high strain rate forming, and processing are widely adopted, such as, high speed cutting and impact hydroforming [13–15]. On the

other hand, with the wider use of aluminum alloy components, high strain rate deformation in extreme conditions (elevated or cryogenic temperature) occurs frequently during their service. However, it is concluded that the mechanical properties under high strain rate deformation usually differ from those under static deformation [16]. Therefore, it is necessary to investigate the dynamic mechanical response of the Al-Mg-Si alloy. A remarkable increment of flow stress of AA 6061-T6 is noted when the strain rate exceeds $1 \times 10^3 \text{ s}^{-1}$ [17]. The work hardening of AA 6061-T6 during deformation is associated with strain rate [18]. Vilamosa et al. [9] found that the mechanical properties of the studied Al-Mg-Si alloys are sensitive to temperature and strain rate. The temperature has obvious effects on the strain rate sensitivity. Acharya et al. [19] investigated the mechanical properties of the studied Al 6061-T6 alloys at high strain rates, and the results show that both strain rate sensitivity and work hardening are related to the strain rate. The previous works are valuable in material selection and structure design, but most of the studies are mainly focused on room temperature deformation. It is worthwhile to make a consideration of dynamic deformation behavior at a wider range of temperatures.

The mechanical property is highly related to the microstructure evolution [20]. When deformed at different conditions, the great evolution of microstructure results in corresponding changes of the mechanical properties [21]. Zhang et al. [22] proved that the aging condition has prominent effect on the mechanical properties of the 6005 alloy aluminum, which can be explained by the different strengthening effects of the precipitates with various types, dimensions, and densities. Ye et al. [23] found that the heat treatment has an obvious influence on the microstructure of 6063 alloy aluminum, which results in different strain rate sensitivities. The evolution of the dislocation and grain size, dynamic precipitation and dynamic dissolution, dynamic recrystallization and dynamic recovery, are mainly responsible for the mechanical properties of the aluminum alloys during high temperature deformation. Therefore, a deep understanding of the deformation mechanism as well as an accurate prediction of the deformation behavior for the materials impacted at different conditions are of great benefit in many engineering fields. Up to now, the scientific research on the microstructure evolution of extruded Al-Mg-Si alloys at extreme conditions is limited. Consequently, the study about the microstructure evolution of the Al-Mg-Si under those different deformation conditions is a meaningful work.

The aim of this study is to make insights into the dynamic responses and the corresponding microstructure evolution of extruded 6013-T4 alloy under impact loading at different temperatures. The stress–strain relationship was discussed. The grain, dislocation and precipitate evolution were analyzed. This work offers a comprehensive recognition of the mechanical responses and its related microstructure development during high strain rate impact.

2. Experimental Procedure

The material studied in this work is a commercially produced extruded 6013-T4 aluminum alloy. The chemical composition is shown in Table 1. The material was received in status of extruded bar with a diameter of 25 mm. The cylinder specimens were cut along the extrusion direction. The height and diameter of the specimens are 4 and 8 mm, respectively.

Table 1. The chemical composition of the extruded 6013 alloy (mass fraction, %).

Mg	Fe	Si	Mn	Zn	Cr	Ti	Al
0.95	0.2	0.75	0.35	0.05	0.1	0.1	Bal.

The split Hopkinson pressure bar (SHPB) is widely used to get the mechanical properties of materials under impacting loading. A schematic drawing of the test device is shown in Figure 1. Incident bar and transmitted bar are 1400 mm in length and the length of the striker bar is 200 mm. The striker bar is accelerated by a compressed-air gun to generate a compressive force.

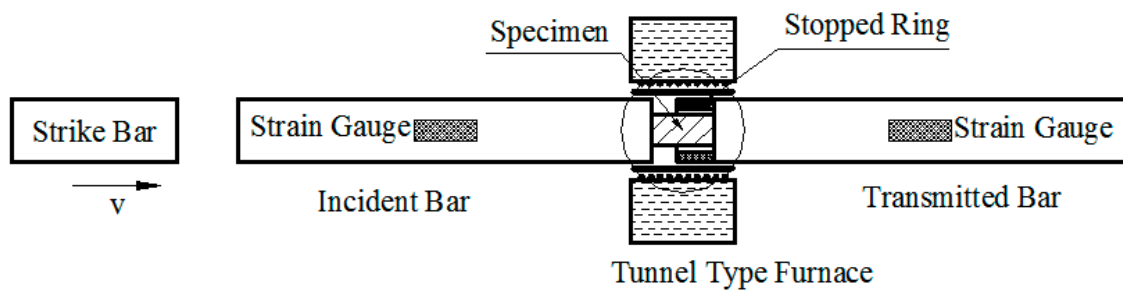


Figure 1. Schematic drawing of a split Hopkinson pressure bar (SHPB) test device.

The true stress, true strain, and the strain rate can be estimated by using the following equations [24]:

$$\sigma = E \frac{A}{A_s} \varepsilon_i, \quad (1)$$

$$\varepsilon = -2 \frac{C_0}{L} \int \varepsilon_r dt, \quad (2)$$

$$\dot{\varepsilon} = -2 \frac{C_0}{L} \varepsilon_r(t), \quad (3)$$

where L is the initial length of the specimen; C_0 ($C_0 = \sqrt{E/\rho}$, here ρ is the mass density of pressure bar) is wave propagation velocity; A and A_s are the cross-sectional areas of the pressure bar and the specimen, respectively; and E is the Young's modulus of the material of the two pressure bars.

In this study, the grease was used to reduce the friction. A thermocouple was applied to detect the test temperature before conducting the compression. The heat furnace was adopted to heat the samples to the proposed temperatures. Then, the specimens were impacted with selected strain rates and strains. The specimens were cooled by dropping them into a water tank as quickly as possible after the impact, aiming to arrest the progress of microstructure. The stopped ring was adopted to ensure a uniform strain in order to make a comparison of the microstructure.

The microstructure observation section for the specimens is shown in Figure 2, which is perpendicular to the compression axis. The original samples were polished before electrolytic etched with Baker's reagent for polarized light optical microscopy observation. As shown in Figure 3, the alloy consists of fibrous grains. After the impact tests, a thin slice was cut from the observation section for the TEM observation. The slice was ground to 0.1 mm in thickness by using abrasive papers. Then, the slice was trepanned in order to get discs with a diameter of 3 mm. Finally, the discs were polished by a twin-jet polishing machine to get a strain free surface with thin thickness. The electrolyte solution consisted of HNO_3 and CH_3OH with ratio of 3:7, the electrolytic voltage was 12 V, and the electrolytic time was about 15 s. The TEM observation was carried out in a G2 F20 transmission electron microscope (FEI, Changsha, China). The corresponding test voltage was 300 kV.

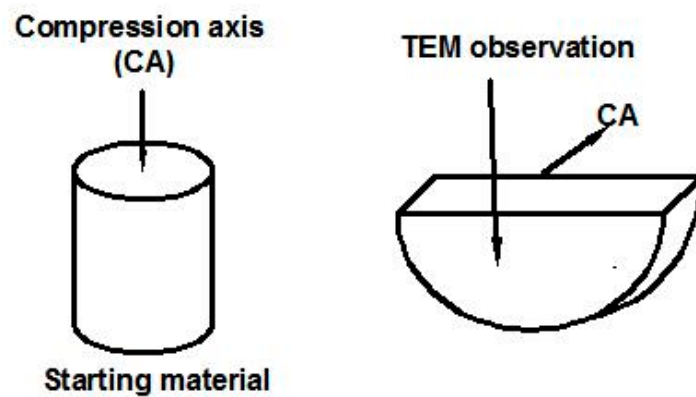


Figure 2. Compression direction and microstructure observation plane.

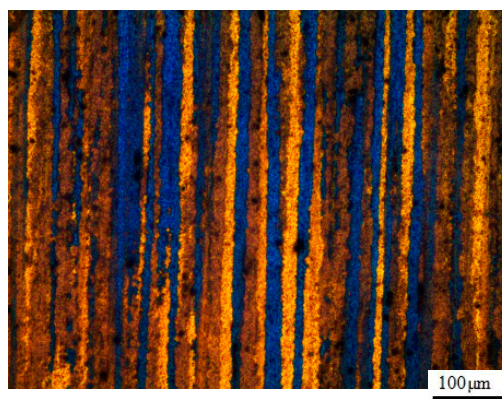


Figure 3. Typical optical microstructure of an extruded 6013-T4 alloy.

3. Results and Discussion

3.1. Stress–Strain Curves

The dynamic true stress–true strain curves for the extruded 6013 aluminum alloy deformed in different temperatures are summarized in Figure 4. The strain rate is ranging from $1 \times 10^3 \text{ s}^{-1}$ to $5 \times 10^3 \text{ s}^{-1}$, respectively. It is obvious that the true stress of the extruded 6013 alloy drops markedly with increasing temperature and increases slightly with the strain rate. When deformed at a certain condition, the true stress increases at a high rate with strain and shows a steady state flow until high strain. The strain hardening behavior is obvious for 6013 alloy, and the strain hardening rate at $400 \text{ }^\circ\text{C}$ is much lower than those of 25 and $200 \text{ }^\circ\text{C}$. It has been explained that the strain hardening for the alloy is attributed to the evolution of the dislocation which includes the increase of dislocation density and the pile-ups of dislocation [25]. At the same time, significant changes will occur for the microstructure of the extruded 6013 aluminum alloy, which also makes great influences on the strain hardening behavior. The stress level of the alloy is affected by the microstructure evolution, therefore, the deformation mechanisms will be deeply discussed in the following part by comparative analysis with microstructural observation.

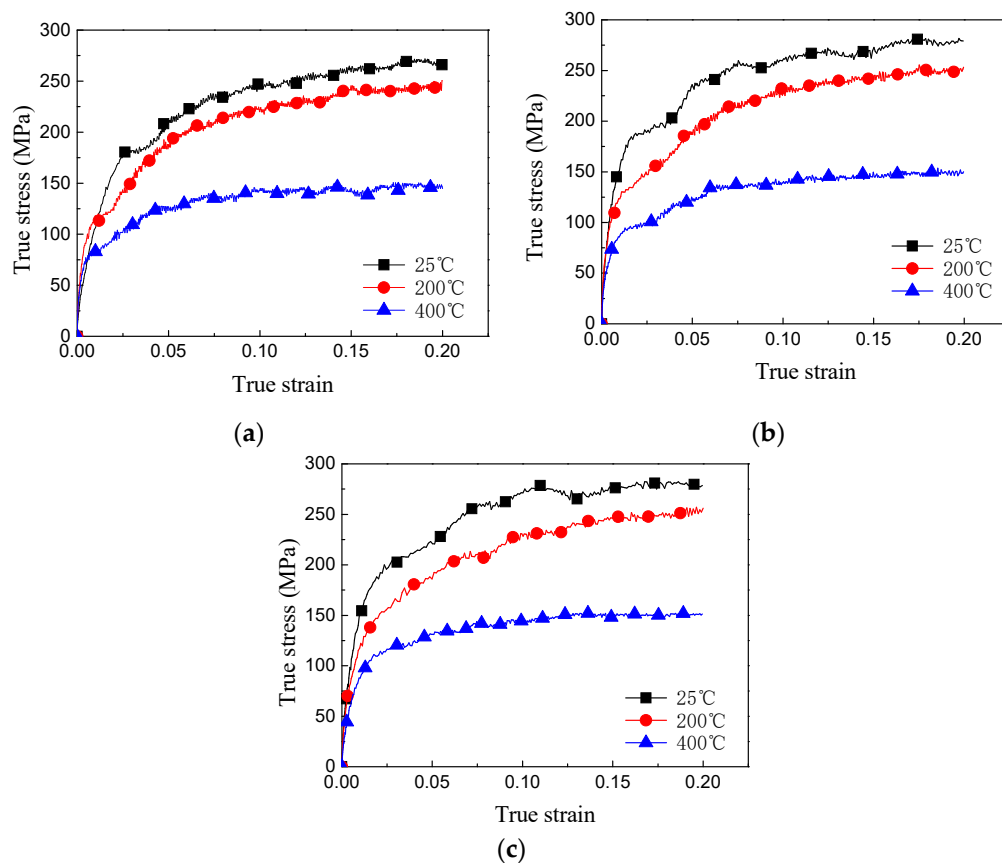


Figure 4. True stress–strain curves of the extruded 6013 alloy impacted at different conditions: (a) 1000 s^{-1} , (b) 3000 s^{-1} , and (c) 5000 s^{-1} .

3.2. Strain Rate Sensitivity

The flow stress dependence on strain rates with various temperatures at a fixed true strain of 0.1 are illustrated in Figure 5. At the strain rates from 1000 to 3000 s^{-1} , the SRS (strain rate sensitivity) declines correspondingly with the increase of the temperature. It is observed that the true stress increases remarkably with strain rate at the temperature of $25\text{ }^{\circ}\text{C}$. However, when deformed at $400\text{ }^{\circ}\text{C}$, the slope becomes moderate. It has been introduced that the SRS is commonly related to the thermal activation under the high strain rate deformation [26]. At strain rates above 3000 s^{-1} , the slopes become gentle and seem to be equal at different temperatures. This may be explained by the fact that the strength effects caused by strain rate hardening and strain hardening of the alloy is counteracted by the thermal softening within the strain rate considered in this study.

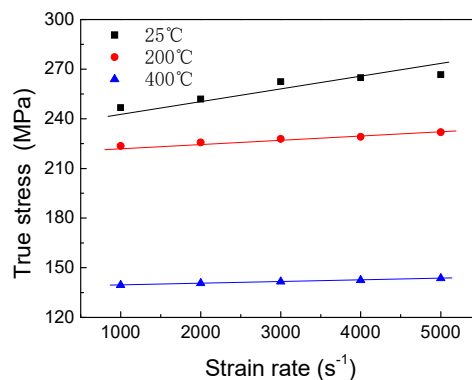


Figure 5. Variation of the flow stress as a function of the strain rate.

3.3. Temperature Sensitivity

The flow stress dependence on temperatures with various strain rates at a fixed true strain of 0.1 is illustrated in Figure 6. As the trend of curves in Figure 6 is similar at all strain rates, it can be concluded that the strain rate has no obvious effect on the temperature sensitivity of the alloy. The flow stresses decrease slightly from 25 to 200 °C, but decrease remarkably with increasing temperature. It is found that planar slip is not fully activated when deformed at room temperature, therefore, the deformation homogeneity and strain hardening exponent are both strengthened [27]. During high temperature impact, grain transformation, dislocation evolution, dynamic precipitation and dissolution are involved in the thermal and severe deformation. These microstructure evolutions lead to a great change of the true stress. Although high strain rate deformation can enhance the strength of the material, it is obvious that the softening effect caused by temperature rise and microstructure evolution deformation is dominant resistance in the high temperature impact of the 6013-T4 alloy.

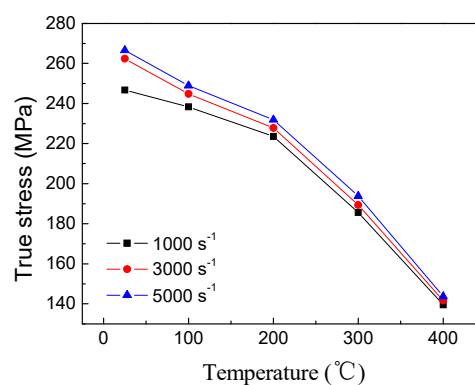


Figure 6. Relationships between true stress and temperature.

3.4. Evolution of the Microstructure

The microstructure evolution of the deformed alloy was studied through TEM observations. The most important structural feature that directly relates to the deformation processing is the dislocation. The TEM images of the specimens compressed at room temperature with different impact conditions are shown in Figure 7. The specimen deformed at the strain rate of 3000 s⁻¹ with a strain of 0.25. Several numbers of dislocation lines are found in Figure 7a, and the density of the dislocation is not high due to the limited strain. Figure 7b shows that the alloy exhibited higher density of dislocations with dislocation tangling and developing cellularity after compression at the strain of 0.5. When the strain reaches 0.75, a high dislocation density with a uniform distribution is detected in Figure 7c, suggesting that the increasing strain hardening effects at room temperature is a consequence of dislocation accumulation, which has been reported previously [27]. From Figure 7b,d we can conclude that the density of the dislocation increases with strain rate at a certain strain, and during dynamic impact the motion of the dislocation is limited, which results in the pile-up of the dislocations.

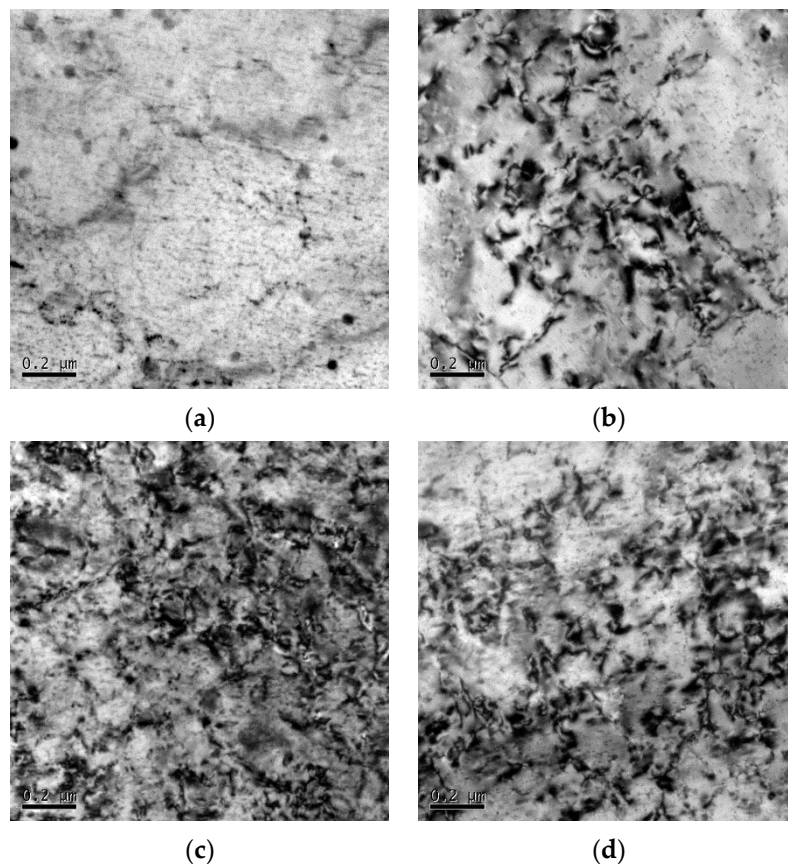


Figure 7. TEM observations of the specimens impacted at 25 °C with various strain and strain rate conditions: (a) 0.25, 3000 s⁻¹, (b) 0.5, 3000 s⁻¹, (c) 0.75, 3000 s⁻¹, (d) 0.5, 5000 s⁻¹.

Figure 8 shows the microstructure evolution of the alloy impacted at the temperature of 200 °C. It is clear that the density of the dislocation increases with the strain (Figure 8a–c). Meanwhile, large numbers of precipitates are observed in the deformed samples. As shown in in Figure 8b the needle-like β'' precipitates are distributed regularly in the impacted specimen as previously reported [22], and these precipitates can pin the dislocations and impede the motion of dislocation during deformation. However, the interaction of precipitate and dislocation becomes moderate as the temperature increases. As illustrated in Figure 8c, only a few needle-like precipitates can be clearly detected due to the high density of dislocations. In previous research [28], the dissolution of β'' precipitates was observed during severe plastic deformation. During the impact deformation, the dislocations and other defects around the precipitates play a role of diffusion channel for the solute atom [29]. Meanwhile, high strain rate can improve the diffusion rate of the solute atom. However, the dissolving phenomenon is not obvious in this work and needs further study. Meanwhile, with the increasing strain rate, some precipitates are distorted due to the plastic deformation. The density number of the precipitate is in a downward trend as shown in Figure 8d.

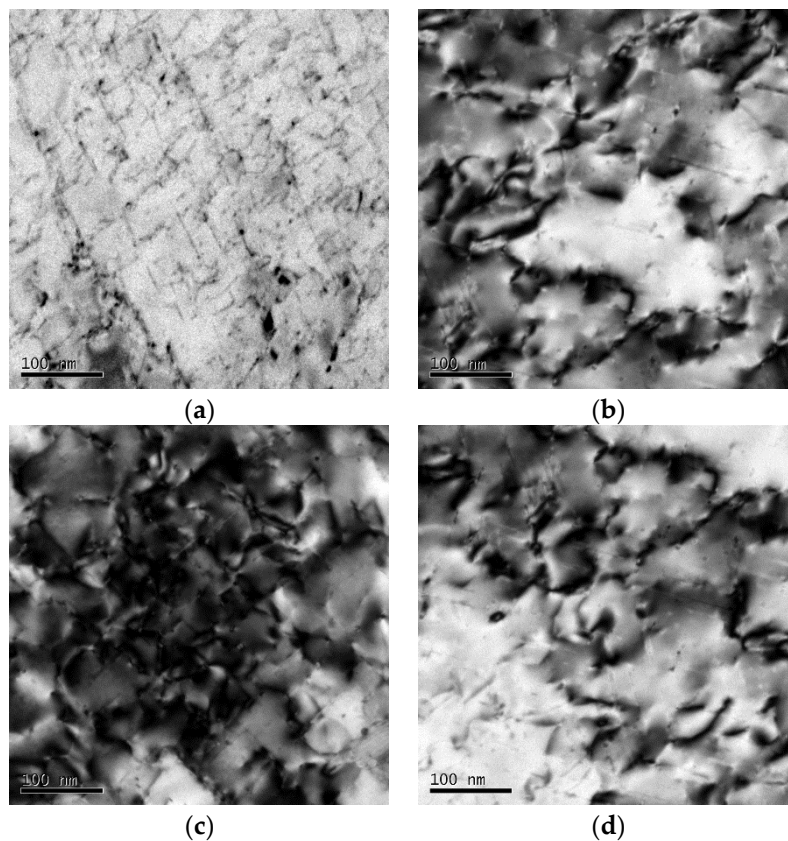


Figure 8. TEM observations of the specimens impacted at 200 °C with various strain and strain rate conditions: (a) 0.25, 3000 s⁻¹, (b) 0.5, 3000 s⁻¹, (c) 0.75, 3000 s⁻¹, (d) 0.5, 5000 s⁻¹.

The transmission electron micrographs of the alloy deformed at 400 °C under different strains and strain rates are exhibited in Figure 9. As shown in Figure 9a, the density of the dislocation is not high with a strain of 0.25, the precipitate becomes coarse with a larger dimension, and distributes with no regulation. This precipitate was characterized as the Q phase in previous research [30]. It has been found that the coarse precipitates result in a decrease of the pinning force to the dislocations [31]. The deformation with higher strain can promote the coarsening process of the precipitate due to Ostwald ripening [32]. It is worth noting that the heat process of the sample at the targeted temperature also has an effect on the precipitation evolution. With increasing of the strain, at the strain of 0.5, the coarser precipitates are still observed clearly (Figure 9b). However, as the strain reaches 0.75, some of the coarse precipitates can still be observed (Figure 9c). From Figure 9a–c we can find that the dislocation density increases with the applied strain. The increment of the temperature accelerates the rate of dislocation annihilation, subsequently resulting in a decline of true stress. However, the coarse precipitate is still recorded, as the applied strain rate goes up from 3000 to 5000 s⁻¹ (Figure 9d). The high strain rate deformation can improve of strength the material due to the accumulation of dislocations. The coarse behavior of the precipitate is assumed to make a contribution to the softening phenomenon during dynamic compression of the extruded 6013 alloy.

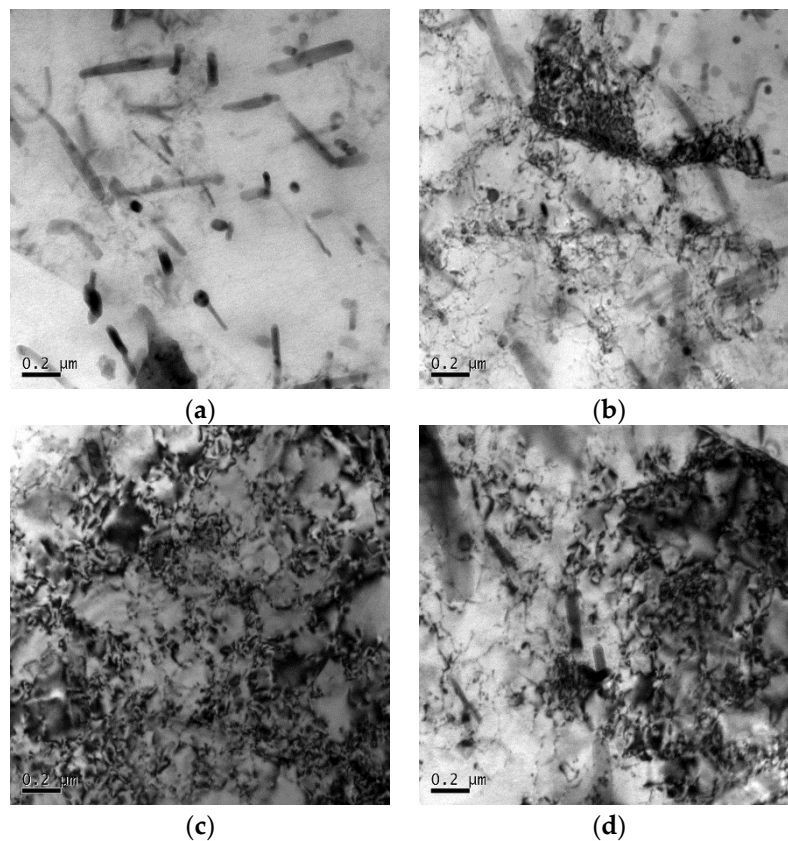


Figure 9. TEM observations of the specimens impacted at 400 °C with various strain and strain rate conditions: (a) 0.25, 3000 s⁻¹, (b) 0.5, 3000 s⁻¹, (c) 0.75, 3000 s⁻¹, (d) 0.5, 5000 s⁻¹.

4. Conclusions

High strain rate compression tests on the extruded 6013-T4 alloy were conducted to explore the influences of strain rate and temperature on the mechanical properties and microstructure evolution. The main findings and conclusions are as following:

(1) Both the strain rate and temperature have an influence on the mechanical properties of the alloy. The stress level increases slightly with increasing strain rate and decreases remarkably with temperature.

(2) When deformed at 25 °C, the density of the dislocation increases with strain, and strain rate leads to a high stress level. However, the density of the dislocation declines with the ascent of deformation temperature. When deformed at 200 °C, the needle-like precipitates were found. The density of dislocation increases with strain and strain rate, and the precipitates can still be observed after impact deformation. When impacted at 400 °C, it was noticed that the density of the dislocation increases with strain and strain rate. Meanwhile, the coarse precipitates were detected, and even the material experienced a large deformation with high strain rate.

Author Contributions: Data curation, W.L. and B.D.; Formal analysis, T.Y.; Funding acquisition, A.L.; Investigation, Y.W.; Project administration, L.L.; Resources, A.L.; Writing—original draft, T.Y.; Writing—review and editing, L.L.

Funding: The authors are very grateful for the support received from the National Key Research and Development Program of China [No. 2016YFB0101700], the Natural Science Foundation of Hunan province (No. 2019JJ30009 2018JJ4031 and 2019JJ50110).

Conflicts of Interest: The authors declare no conflict of interest.

References

1. Zhu, B.; Li, L.; Liu, X.; Zhang, L.; Xu, R. Effect of viscosity measurement method to simulate high pressure die casting of thin-wall AlSi10MnMg alloy castings. *J. Mater. Eng. Perform.* **2015**, *24*, 5032–5036. [[CrossRef](#)]
2. Viceré, A.; Roventi, G.; Paoletti, C.; Cabibbo, M.; Bellezze, T. Corrosion behavior of AA6012 aluminum alloy processed by ECAP and cryogenic treatment. *Metals* **2019**, *9*, 408. [[CrossRef](#)]
3. Panagopoulos, C.; Georgiou, E.; Giannakopoulos, K.; Orfanos, P. Effect of pH on stress corrosion cracking of 6082 Al alloy. *Metals* **2018**, *8*, 578. [[CrossRef](#)]
4. Pogatscher, S.; Antrekowitsch, H.; Leitner, H.; Ebner, T.; Uggowitzner, P.J. Mechanisms controlling the artificial aging of Al–Mg–Si alloys. *Acta Mater.* **2011**, *59*, 3352–3363. [[CrossRef](#)]
5. Wang, K.; Li, J.; Stoughton, T.B.; Carsley, J.E.; Carlson, B.E. Effect of preform annealing on plastic anisotropy of an age-hardenable Al–Mg–Si alloy. *J. Mater. Process. Technol.* **2018**, *252*, 381–388. [[CrossRef](#)]
6. Ding, L.; Weng, Y.; Wu, S.; Sanders, R.E.; Jia, Z.; Liu, Q. Influence of interrupted quenching and pre-aging on the bake hardening of Al–Mg–Si Alloy. *Mater. Sci. Eng. A* **2016**, *651*, 991–998. [[CrossRef](#)]
7. Gilioli, A.; Manes, A.; Giglio, M.; Wierzbicki, T. Predicting ballistic impact failure of aluminium 6061-T6 with the rate-independent Bao–Wierzbicki fracture model. *Int. J. Impact. Eng.* **2015**, *76*, 207–220. [[CrossRef](#)]
8. Donatus, U.; Thompson, G.E.; Zhou, X.; Wang, J.; Cassell, A.; Beamish, K. Corrosion susceptibility of dissimilar friction stir welds of AA5083 and AA6082 alloys. *Mater. Charact.* **2015**, *107*, 85–97. [[CrossRef](#)]
9. Zhao, Y.; Song, B.; Pei, J.; Jia, C.; Li, B.; Linlin, G. Effect of deformation speed on the microstructure and mechanical properties of AA6063 during continuous extrusion process. *J. Mater. Process. Technol.* **2013**, *213*, 1855–1863. [[CrossRef](#)]
10. Vilamosa, V.; Clausen, A.H.; Børvik, T.; Skjervold, S.R.; Hopperstad, O.S. Behaviour of Al–Mg–Si alloys at a wide range of temperatures and strain rates. *Int. J. Impact. Eng.* **2015**, *86*, 223–239. [[CrossRef](#)]
11. Fjeldbo, S.K.; Li, Y.; Marthinsen, K.; Furu, T. Through-process sensitivity analysis on the effect of process variables on strength in extruded Al–Mg–Si alloys. *J. Mater. Process. Technol.* **2012**, *212*, 171–180. [[CrossRef](#)]
12. Ye, T.; Wu, Y.; Liu, A.; Xu, C.; Li, L. Mechanical property and microstructure evolution of aged 6063 aluminum alloy under high strain rate deformation. *Vacuum* **2019**, *159*, 37–44. [[CrossRef](#)]
13. He, Y.; Zhang, J.; Qi, Y.; Liu, H.; Memon, A.R.; Zhao, W. Numerical study of microstructural effects on chip formation in high speed cutting of ductile iron with discrete element method. *J. Mater. Process. Technol.* **2017**, *249*, 291–301. [[CrossRef](#)]
14. Zhang, P.; Wang, Y. Effects of shear strain and annealing on the nano-precipitate phase and crystal orientation of 7055 aluminum alloy during cutting process. *Vacuum* **2018**, *151*, 247–253. [[CrossRef](#)]
15. Zhang, F.; Li, X.; Xu, Y.; Chen, J.; Chen, J.; Liu, G.; Yuan, S. Simulating sheet metal double-sided hydroforming by using thick shell element. *J. Mater. Process. Technol.* **2015**, *221*, 13–20. [[CrossRef](#)]
16. Ma, H.; Huang, L.; Tian, Y.; Li, J. Effects of strain rate on dynamic mechanical behavior and microstructure evolution of 5A02-O aluminum alloy. *Mater. Sci. Eng. A* **2014**, *606*, 233–239. [[CrossRef](#)]
17. Manes, A.; Serpellini, F.; Pagani, M.; Saponara, M.; Giglio, M. Perforation and penetration of aluminium target plates by armour piercing bullets. *Int. J. Impact. Eng.* **2014**, *69*, 39–54. [[CrossRef](#)]
18. Lee, W.S.; Liu, M.H. Effects of directional grain structure on impact properties and dislocation substructure of 6061-T6 aluminium alloy. *Mater. Sci. Technol.* **2014**, *30*, 1719–1727. [[CrossRef](#)]
19. Acharya, S.; Gupta, R.K.; Ghosh, J.; Bysakh, S.; Ghosh, K.S.; Mondal, D.K.; Mukhopadhyay, A.K. High strain rate dynamic compressive behaviour of Al6061-T6 alloys. *Mater. Charact.* **2017**, *127*, 185–197. [[CrossRef](#)]
20. Lee, W.S.; Tang, Z.C. Relationship between mechanical properties and microstructural response of 6061-T6 aluminum alloy impacted at elevated temperatures. *Mater. Des.* **2014**, *58*, 116–124. [[CrossRef](#)]
21. Zhang, P.; Wang, Y. Effects of heat treatment on the nanoscale precipitation behavior of 7055 aluminum alloy under dynamic shock. *Vacuum* **2018**, *152*, 150–155. [[CrossRef](#)]
22. Zhang, L.; He, H.; Li, S.; Wu, X.; Li, L. Dynamic compression behavior of 6005 aluminum alloy aged at elevated temperatures. *Vacuum* **2018**, *155*, 604–611. [[CrossRef](#)]
23. Ye, T.; Li, L.; Guo, P.; Xiao, G.; Chen, Z. Effect of aging treatment on the microstructure and flow behavior of 6063 aluminum alloy compressed over a wide range of strain rate. *Inter. J. Impact. Eng.* **2016**, *90*, 72–80. [[CrossRef](#)]
24. Ramezani, M.; Ripin, Z.M. Combined experimental and numerical analysis of bulge test at high strain rates using split Hopkinson pressure bar apparatus. *J. Mater. Process. Technol.* **2010**, *210*, 1061–1069. [[CrossRef](#)]

25. Tiamiyu, A.A.; Badmos, A.Y.; Odeshi, A.G. Effects of temper condition on high strain-rate deformation of AA 2017 aluminum alloy in compression. *Mater. Des.* **2016**, *89*, 872–883. [[CrossRef](#)]
26. Lee, W.S.; Sue, W.C.; Lin, C.F.; Wu, C.J. The strain rate and temperature dependence of the dynamic impact properties of 7075 aluminum alloy. *J. Mater. Process. Technol.* **2000**, *100*, 116–122. [[CrossRef](#)]
27. Evers, L.P.; Parks, D.M.; Brekelmans, W.A.M.; Geers, M.G.D. Crystal plasticity model with enhanced hardening by geometrically necessary dislocation accumulation. *J. Mech. Phys. Solids.* **2002**, *50*, 2403–2424. [[CrossRef](#)]
28. Cabibbo, M.; Evangelista, E.; Vedani, M. Influence of severe plastic deformations on secondary phase precipitation in a 6082 Al-Mg-Si alloy. *Metall. Mater. Trans. A* **2005**, *36*, 1353–1364. [[CrossRef](#)]
29. Sun, D.; Zhang, X.; Ye, L.; Gu, G.; Jiang, H.; Gui, X. Evolution of θ' precipitate in aluminum alloy 2519A impacted by split Hopkinson bar. *Mater. Sci. Eng. A* **2015**, *620*, 241–245. [[CrossRef](#)]
30. Fan, X.; Li, M.; Li, D.; Shao, Y.; Zhang, S.; Peng, Y. Dynamic recrystallisation and dynamic precipitation in AA6061 aluminium alloy during hot deformation. *Mater. Sci. Technol.* **2014**, *30*, 1263–1272. [[CrossRef](#)]
31. Yang, Q.; Dong, D.; Zhang, Z.; Cao, L.; Wu, X.; Huang, G.; Liu, Q. Flow behavior and microstructure evolution of 6A82 aluminium alloy with high copper content during hot compression deformation at elevated temperatures. *Trans. Nonferr. Metal. Soc.* **2016**, *26*, 649–657. [[CrossRef](#)]
32. Liu, S.; You, J.; Zhang, X.; Deng, Y.; Yuan, Y. Influence of cooling rate after homogenization on the flow behavior of aluminum alloy 7050 under hot compression. *Mater. Sci. Eng. A* **2010**, *527*, 1200–1205. [[CrossRef](#)]



© 2019 by the authors. Licensee MDPI, Basel, Switzerland. This article is an open access article distributed under the terms and conditions of the Creative Commons Attribution (CC BY) license (<http://creativecommons.org/licenses/by/4.0/>).